Check for updates

Angewandte Chemie International Edition

Angewandte International Edition Chemie

How to cite: *Angew. Chem. Int. Ed.* **2026**, 65, e7839925
doi.org/10.1002/anie.7839925

RESEARCH ARTICLE

Reactant-Transporting Metal-Support Interaction for Lattice Carbonate-to-Methane Catalysis

Guangxing Yang[1,2] | Hanke Li[1,3] | Yiming Niu[4] | Chengxiong Dang[2] | Yonghai Cao[1] | Hongjuan Wang[1] | Hao-Fan Wang[1] | Bingsen Zhang[4] | Feng Peng[2] | Hao Yu[1]

[1]School of Chemistry and Chemical Engineering, South China University of Technology, Guangzhou, P. R. China | [2]School of Chemistry and Chemical Engineering, Guangzhou University, Guangzhou, P. R. China | [3]National Reference Laboratory for Food Contact Material (Guangdong), Guangzhou Customs Technology Center, Guangzhou, P. R. China | [4]Shenyang National Laboratory for Materials Science, Institute of Metal Research, Chinese Academy of Sciences, Shenyang, P. R. China

Correspondence: Hao Yu (yuhao@scut.edu.cn)

Received: 16 February 2026 | **Revised:** 3 April 2026 | **Accepted:** 13 April 2026

Keywords: hydrogenation | lattice carbonate | methane | reactant-transporting metal-support interaction

ABSTRACT

As a core concept of heterogeneous catalysis, metal-support interactions are pivotal controlling activity, selectivity, and stability via electronic and geometric effects. Here, we report a reactant-transporting form of metal support interaction (MSI), named as strong metal-reactive support interaction (SMRSI) where Pt/H_2 directly hydrogenates lattice carbonate in calcite to CH_4 with ≤ 415 °C onset and ~98% selectivity (390–510°C). Because lattice carbon in carbonate minerals constitutes Earth's largest carbon reservoir, enabling low-temperature lattice–carbonate conversion offers a catalytic lever to accelerate the slow carbon cycle (ACC) complementary to fast carbon cycle (FCC)-based CO_2 management. Operando techniques show a permeable amorphous interphase that dynamically encapsulates Pt, transports CO_3^{2-} to active sites, and crystallizes into $Ca(OH)_2$, thereby sustaining a mobile triple-phase boundary, where carbonate-derived *CO intermediate was hydrogenated to CH_4. It is resolved that a low-temperature interfacial CO_2 release is diagnostic of boundary decomposition. Kinetics separate a CO_3^{2-}-diffusion-limited solid-state path at low temperatures from a high-temperature route akin to gaseous-CO_2 hydrogenation. The hydrogenated solid is re-carbonated by CO_2, regenerating $CaCO_3$ and retaining selectivity over cycles. Conceptually, the SMRSI extends MSI from electronic/geometric tuning to reactant transport, illustrating how moving solid-solid@gas interfaces mediate transformations of solid reactants.

1 | Introduction

Lattice carbon, carbon locked in the crystal lattices of carbonate minerals, constitutes Earth's largest and most consequential carbon reservoir within the lithosphere. As illustrated in Figure 1a, the fast carbon cycle (FCC) circulates ~10–100 Gt C yr^{-1} through photosynthesis–respiration–combustion, whereas the slow carbon cycle (SCC) turns over only ~0.01–0.1 Gt C yr^{-1} despite holding this dominant inventory [1]. Today, anthropogenic use of fossil carbon (~9.6 Gt C yr^{-1}) now exceeds the FCC's assimilation capacity (~4.4 Gt C yr^{-1}), leaving ~5.2 Gt C to accumulate in the atmosphere annually. This imbalance elevates carbonate conversion from a geological curiosity to a catalytic imperative: if we can activate lattice carbonate at low temperature and couple hydrogenation with re-carbonation, we can accelerate the SCC, defined as an accelerated carbonate cycle (ACC), and create a complementary, mineral-anchored pathway for durable CO_2 management (Figure 1b).

[Correction added on 05 September 2026, The order of the affiliation numbers was corrected.]

© 2026 Wiley-VCH GmbH

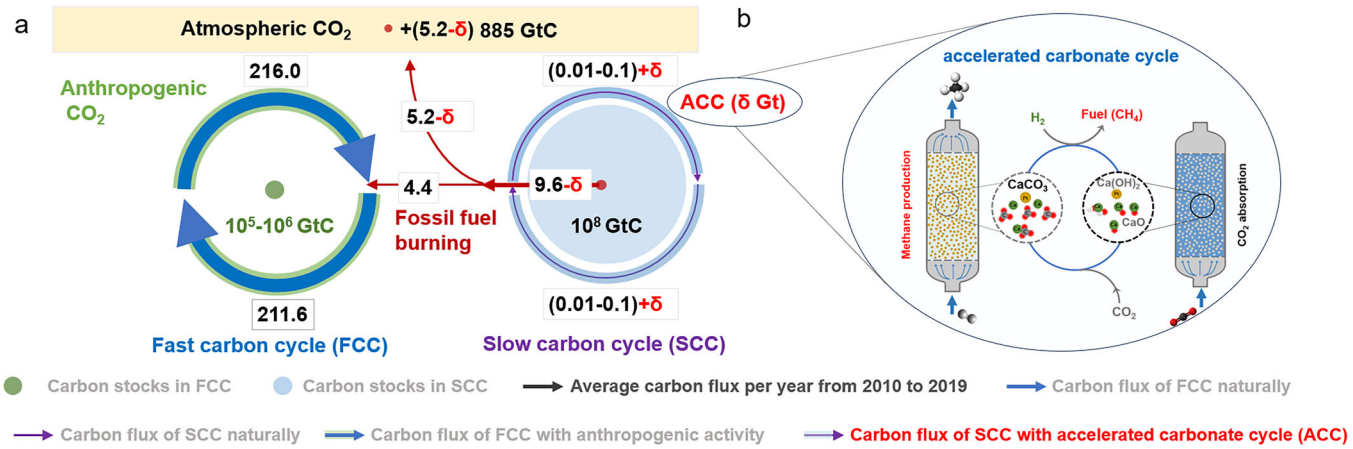

FIGURE 1 | A simplified pictorial illustration of the global carbon cycle in nature. (a) Fast and slow carbon cycles in the Earth [2] with/without (b) accelerated carbonate cycle in the slow carbon cycle of lithosphere.

To address the imbalance between CO_2 emissions and removal, direct air capture (DAC) technologies and subsequent utilization have been developed and have garnered growing interest [3–6]. Here, we target the slow carbon cycle directly by using the lithospheric lattice carbonate reservoir as feedstock rather than managing released CO_2. Carbonate minerals naturally digest CO_2 via weathering but on geological timescales [7, 8]; an ACC is instead proposed in which green H_2 hydrogenates calcite ($CaCO_3$) to CH_4 while generating $CaO/Ca(OH)_2$, followed by CO_2-driven re-carbonation that regenerates $CaCO_3$ [9, 10]. Because CaO readily captures CO_2 and H_2O to form $Ca(OH)_2$/carbonate, this mineral–fuel–mineral loop can operate under moderate conditions, displacing fossil methane and curbing net atmospheric CO_2. The techno-economic study provides a detailed evaluation of this process, demonstrating that the integrated carbon capture and conversion (ACC) process exhibits economic competitiveness when capital costs, operational expenses, and carbon credits are taken into account [11]. Within this framework, the central scientific challenge and the focus of this work is to activate and transport lattice carbonate to metal sites at solid–solid@gas boundaries to sustain continuous conversion [12, 13].

Against this backdrop, two mechanistic routes have been invoked for carbonate-to-fuel chemistry. Thermal decomposition in inert gas produces metal oxides plus CO_2, which can then be hydrogenated, but this pathway is energy intensive [14–18]. In H_2 atmospheres, alkaline-earth carbonates can be converted in situ at lower temperatures [12, 19–28]. Whether hydrocarbons arise by direct hydrogenation of surface carbonate [10, 29], via hydrogenation of CO_2 released from carbonate remains debated [9], or through hydrogen spillover from metal sites to carbonate surface remains debated. Recent studies further show that CaO generated from $CaCO_3$ can act as a self-catalyst for H_2 activation and CO formation at $CaO/CaCO_3$ interfaces [12, 30]. Incorporating transition metals (Fe, Co, Ni) lowers temperatures and improves CH_4 selectivity, but reactions occur at complex, dynamic interfaces among carbonates, nascent oxides/hydroxides, and gas [24, 25, 27, 28, 31–33]. While hydrogen spillover, the migration of dissociated H atoms from metal nanoparticles onto oxide or carbonate supports, has been proposed to promote hydrogenation, this pathway generally relies on strong metal–support interactions and sufficient hydrogen dissociation capability of the support itself [34, 35]. However, in the context of direct carbonate hydrogenation, hydrogen migration becomes highly unfavorable, especially over non-reducible supports such as MgO [36] or Al_2O_3 [37]. Considering the physicochemical similarity between CaO and non-reducible oxides such as MgO for which H-atom migration barriers are high, the activation barrier on CaO is expected to be prohibitively high, effectively precluding a spillover mechanism in this system. Crucially, we still lack a framework for how lattice CO_3^{2-} is mobilized and delivered to metal sites across moving solid–solid@gas boundaries; for example, $Ni/BaCO_3$ enriches interfacial gaseous CO_2 for methanation rather than transporting lattice carbonate to the metal [24, 32, 38–41].

Realizing this loop requires mobile, permeable metal–carbonate interfaces; otherwise, accumulated $CaO/Ca(OH)_2$ product layers passivate the metal and stall conversion. Yet the physics of these moving solid–solid@gas boundaries remain a black box, largely because suitable operando characterization and predictive models for solid-reactant transport are scarce [42, 43]. As in classic solid-state demonstrations (e.g., MnO_2-catalysed $KClO_3$ decomposition), intermediates and anion-transport pathways are typically inferred rather than directly observed [42, 43]. Recent advances in reactive strong metal support interaction (SMSI) begin to visualize dynamic overlayers, but they primarily show porous carbonate coatings on Ni that stabilize metal and enrich interfacial gaseous CO_2, facilitating CO_2 methanation rather than delivering lattice CO_3^{2-} to metal sites for direct solid-state hydrogenation. This gap underscores the need for a framework that couples interfacial mobility with lattice-carbonate activation and transport, which we establish here.

To resolve this long-standing ambiguity, we focus on the dual role of carbonate, as both reactive lattice CO_3^{2-} reservoir and metal support, and posit that sustained conversion requires an interface that activates and transports lattice carbonate to metal sites while continuously clearing product layers. Here, we introduce a reactant-transporting metal–support interaction at moving solid–solid@gas boundaries: under H_2, a permeable amorphous interphase dynamically encapsulates Pt, shuttles lattice CO_3^{2-} to the metal where it forms carbonate-derived CO then is hydrogenated to CH_4, and evolves into $Ca(OH)_2$/CaO that is subsequently re-carbonated under CO_2. This framework contrasts

15213773, 2026, 24, Downloaded from https://onlinelibrary.wiley.com/doi/10.1002/anie.783992 5 by Yonghai Cao - South China University Of Technology , Wiley Online Library on [17/11/2026]. See the Terms and Conditions (https://onlinelibrary.wiley.com/terms-and-conditions) on Wiley Online Library for rules of use; OA articles are governed by the applicable Creative Commons License

with reactive SMSI in CO_2 methanation (e.g., Ni/$BaCO_3$), where porous carbonate overlayers primarily enrich interfacial gaseous CO_2 rather than deliver lattice carbonate to metal sites, thereby filling a theoretical and methodological gap in solid–solid@fluid catalysis, including CO_2 hydrogenation, where surface carbonates form [39, 44], and the solid electrolyte–electrode interfaces in lithium–sulfur (Li–S) batteries [45].

2 | Results and Discussion

2.1 | Hydrogenation of Calcite

To explore how lattice carbonate is activated and delivered to metal sites at dynamic solid–solid@gas boundaries, we prepared a family of metal/carbonate catalysts designed for high interfacial density including Fe, Co, Ni, Cu, Pt, Ru, Rh, and Pd supported on $CaCO_3$ (Figure S1). Product selectivity varied systematically with the metal identity (Figure S1), with Pt and Ni favoring CH_4 while Cu, Fe and Ru predominantly produced CO. This metal-dependent selectivity persists across different temperature regimes: at lower temperatures (390–415°C), Ni, Pt, Rh, and Pd exhibit high CH_4 selectivity, whereas CO formation becomes dominant above 530°C on Pt, Rh Ru, and Pd. The temperature-dependence of selectivity can be rationalized by the shift of hydrogenation thermodynamic equilibrium of carbonate (Figure S4). From kinetics perspective, the relatively low barrier for CO formation and facile desorption of CO facilitate the selectivity of CO. Moreover, the decreased hydrogen coverage will also reduce the availability of *H for CO hydrogenation at high temperatures. Those factors lead to the dominant formation of CO above 530°C on Pt, Ru, Rh, Pd [46]. This metal dependence is unexpected for a mechanism based on hydrogen spillover followed by hydrogenation on the carbonate surface, which would yield metal-independent product distributions. Instead, the selectivity trends mirror each metal's intrinsic CO hydrogenation properties, indicating that the final hydrogenation step occurs on metal sites. This observation, coupled with geometric confinement at the three-phase boundary and solid-state carbonate decomposition kinetics, supports a solid-solid@gas interfacial catalysis, which we discuss in detail below [13].

To interrogate reactant-transporting MSI most cleanly, we selected Pt/$CaCO_3$ as a model system because it combines low-temperature activity with high CH_4 selectivity. In addition, Pt exhibits superior stability against sintering and coking under reaction conditions, provides well-defined DRIFTS signals for in situ mechanistic tracking, and allows for the synthesis of uniform nanoparticles that maximize Pt–carbonate interfacial contact. The model catalyst comprises Pt nanoparticles (4.9 ± 1.1 nm) at 3.17 wt% loading dispersed on $CaCO_3$ (Figure S2). Given the support's BET of 3.53 $m^2\ g^{-1}$, hemispherical particles of Pt at this size cover ~ 27.9% of the $CaCO_3$ surface (Supporting Text), ensuring abundant Pt|$CaCO_3$ interfaces to probe interfacial mobility and carbonate delivery. In H_2, $CaCO_3$ conversion initiates at 535 °C, far below that in N_2 (Figures S3–S4), reflecting the favorable thermodynamics of hydrogen-assisted decarbonation. Decorating $CaCO_3$ with Pt lowers the onset to 415 °C, demonstrating a kinetic promotion by the metal. Increasing H_2 partial pressure further decreases the onset (Figure S5), consistent with H_2-driven enhancement of the chemical-potential gradient that sustains boundary decomposition and carbonate flux. Temperature-programmed analysis (Figures S5 and S6) shows efficient conversion of $CaCO_3$ to CH_4 and CO. Under 5 mL min^{-1} H_2, CH_4 selectivity of ~98% is maintained across 390–510 °C. Higher H_2 flow rates shift conversion to lower temperatures but dilute CH_4 in the effluent. After hydrogenation, the solids are re-carbonated under CO_2 to regenerate Pt/$CaCO_3$, sustaining 5%–6% conversion and 95%–98% CH_4 selectivity over ten H_2↔CO_2 cycles (Figure S7). The system demonstrates significant techno-economic appeal for implementing the ACC mineral-fuel-mineral loop, with its feasibility strongly driven by the use of an inexpensive catalyst and affordable green hydrogen [11]. X-ray absorption spectra show no change in Pt valence/coordination after hydrogenation (Figure S8); only slight particle growth is observed after repeated cycling (Figure S9). The wide temperature range for high-selectivity CH_4 production, the notably low conversion temperature compared to direct $CaCO_3$ decomposition, and the stable cyclability suggest that Pt-catalyzed hydrogenation of calcite minerals offers a promising refinery approach for fuel production.

2.2 | In Situ Identification of Structure and Surface Species

Under H_2, the $CaCO_3$ diffraction intensity decays continuously while $Ca(OH)_2$ and then CaO emerge (Figure 2a). Rietveld analysis (Figures 2b and S10) quantifies a $Ca(OH)_2$ maximum between 350°C and 430 °C, in line with the calculated thermodynamic stability window (Figure S4), followed by onset of CaO at ~410 °C and full conversion at higher temperatures. Ex situ XRD (Figure S11) confirms that raising temperature accelerates decarbonation to CaO/$Ca(OH)_2$, consistent with an endothermic process. These observations map the interfacial thermodynamics but cannot, by themselves, account for the observed low-temperature methanation. In situ diffuse reflectance infrared Fourier transform spectroscopy (DRIFTS) (Figure 2c) shows linear *CO at ~2050 cm^{-1} from 200 °C, peaking at 300 °C, well below the bulk-decomposition temperature, together with —OH (~3600 cm^{-1}, $Ca(OH)_2$) and CH_4 (~3016 cm^{-1}) (Figure 2c). The apparent scarcity of bulk $Ca(OH)_2$ in XRD while surface —OH persists in DRIFTS indicates short-lived, surface-confined $Ca(OH)_2$ that is rapidly consumed/turned over. In the absence of *d*-block transition metals, H_2 exerts thermodynamic control by continuously consuming CO_2 via the reverse water–gas shift reaction, shifting the equilibrium of equation: $CaCO_3 \rightleftharpoons CaO + CO_2$, toward decomposition following Le Chatelier's principle. H_2 also influences kinetics through direct surface interactions with the carbonate lattice, forming metastable bicarbonate (HCO_3^-) intermediates that significantly lower the CO_2 dissociation energy barrier [30]. The resulting CaO phase serves dually as a reaction product and an active site for H_2 activation, facilitating CO_2 hydrogenation to CO via a formate-mediated pathway [30]. In the presence of Pt, H_2 facilely dissociates and adsorbs onto Pt surfaces at temperatures as low as 50°C, forming Pt—H bonds confirmed by DRIFTS in previous studies [47, 48]. However, the overlap of Pt—H and linearly adsorbed *CO bands complicates *CO analysis at ~2000 cm^{-1} in IR spectroscopy. To resolve this, we replaced H_2 with deuterium (D_2), exploiting isotopic shifts to lower the Pt—D vibrational frequency. This substitution clarifies *CO species identification without Pt—H spectral interference [47–49]. The band at 2030 cm^{-1} for adsorbed *CO initially increases then

15213773, 2026, 24, Downloaded from https://onlinelibrary.wiley.com/doi/10.1002/anie.783992 5 by Yonghai Cao - South China University Of Technology , Wiley Online Library on [17/11/2026]. See the Terms and Conditions (https://onlinelibrary.wiley.com/terms-and-conditions) on Wiley Online Library for rules of use; OA articles are governed by the applicable Creative Commons License

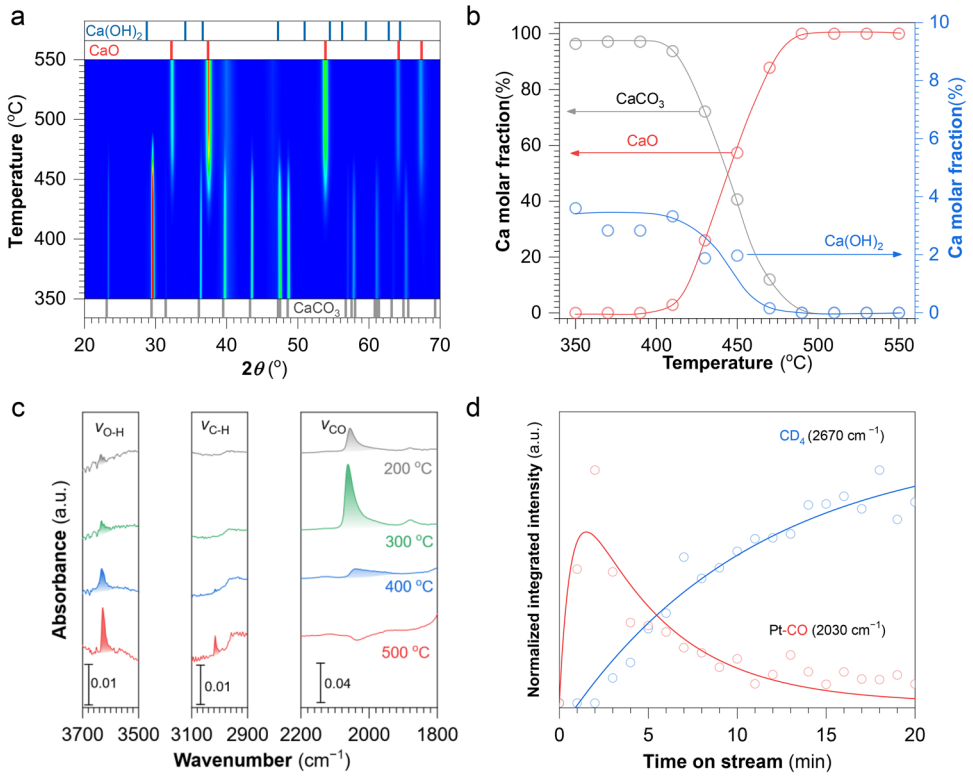

FIGURE 2 | Dynamics changes of bulk materials and surface species. (a) Contour plots of the in situ x-ray diffraction patterns of Pt/$CaCO_3$ at different temperatures under H_2 flow. (b) Molar fraction of solid phase Ca species as a function of temperature. The molar fraction of each species ($CaCO_3$, $Ca(OH)_2$, CaO) was calculated as its mole amount divided by the total moles of calcium species present derived from Rietveld analyses of X-ray diffractograms in (a) and S11. (c) In situ diffuse reflectance infrared Fourier transform spectroscopy (DRIFTS) of Pt/$CaCO_3$ under H_2 at different temperatures. (d) The evolution of intensities of the IR band at 2670 cm^{-1} and 2030 cm^{-1} during deuteration of Pt/$CaCO_3$ under D_2 at 500°C.

decreases during deuteration (Figure 2d), while the band at 2670 cm^{-1} for CD_4 (CH_4 at ~3016 cm^{-1}) rises and levels off, indicating *CO adsorption on Pt sites as an intermediate for CD_4 formation. This isotopic experimental result unambiguously demonstrates sequential hydrogenation from *CO to CH_4 on Pt sites.

2.3 | In Situ Observation of Dynamic Interfaces

In situ transmission electron microscopy (TEM) emerges as a critical technique for resolving these transient structural dynamics at the nanoscale. However, under the electron beam, at a dosage of ~200 e $Å^{-2}$ s^{-1}, $CaCO_3$ rapidly decomposes into CaO and CO_2 in a He atmosphere (Figure S12), leading to the formation of a solid layer over Pt nanoparticles (Figure S13) due to the high surface free energy of Pt than carbonate/oxide, which is the driving force of forming core-shell structure [50, 51]. This self-decomposition, induced by electron radiation, complicates the accurate identification of surface and interface structures of carbonate-containing phases. [52, 53] To suppress artifacts, cryo-TEM was employed to examine the structure of partially hydrogenated Pt/$CaCO_3$, treated in H_2 at 500°C for 2 h [44]. Cryo-TEM images show crystal planes with a *d*-spacing of 0.49 nm, corresponding to the (101) planes of $Ca(OH)_2$, consistent with XRD results. Furthermore, extended x-ray absorption fine structure (EXAFS) analysis reveals an increase in the average Ca—O coordination number from 6 to 9 post-hydrogenation, confirming the formation of $Ca(OH)_2$ and CaO from $CaCO_3$ decarbonization (Figure S14). The $Ca(OH)_2$ crystals (~18 nm) are substantially smaller than the parent $CaCO_3$ grains (~10 μm) (Figure S15), indicating nucleation/renewal at the interface rather than bulk-grain transformation. Notably, $Ca(OH)_2$ consistently forms adjacent to Pt nanoparticles, underscoring the pivotal catalytic role of Pt in $CaCO_3$ hydrogenation. As illustrated in Figure 3b, large $CaCO_3$ grains are transformed into smaller $Ca(OH)_2$ grains, facilitated by Pt, with CH_4 and CO released at the Pt-solid interface.

A simple capacity estimate shows that each 4.9 nm (hemispherical) Pt particle can, upon complete reaction, convert a 0.74×10^6 nm^3 $CaCO_3$ volume, equivalent to a ~30.6 nm hemispherical $CaCO_3$ domain. Even at 5% conversion of carbonate, this domain is ~11.2 nm, larger than the Pt particle (Figure S16). This geometric mismatch rules out a purely static interfacial annulus as the carbon source in cycling tests (Figure S7), implying that carbonate from beyond the immediate contact zone must be transported to the metal.

To observe carbonate transportation towards Pt catalysts, Pt blacks with large grain sizes were physically mixed with $CaCO_3$ for in situ TEM experiments, enabling direct observation of interface formation between Pt and $CaCO_3$. The large Pt grain sizes enhance structural stability under electron irradiation and can weaken the interaction with support compared with small Pt nanoparticle. This configuration provides a sufficiently extended time window to capture the dynamic formation of

15213773, 2026, 24, Downloaded from https://onlinelibrary.wiley.com/doi/10.1002/anie.7839925 by Yonghai Cao - South China University Of Technology , Wiley Online Library on [17/11/2026]. See the Terms and Conditions (https://onlinelibrary.wiley.com/terms-and-conditions) on Wiley Online Library for rules of use; OA articles are governed by the applicable Creative Commons License

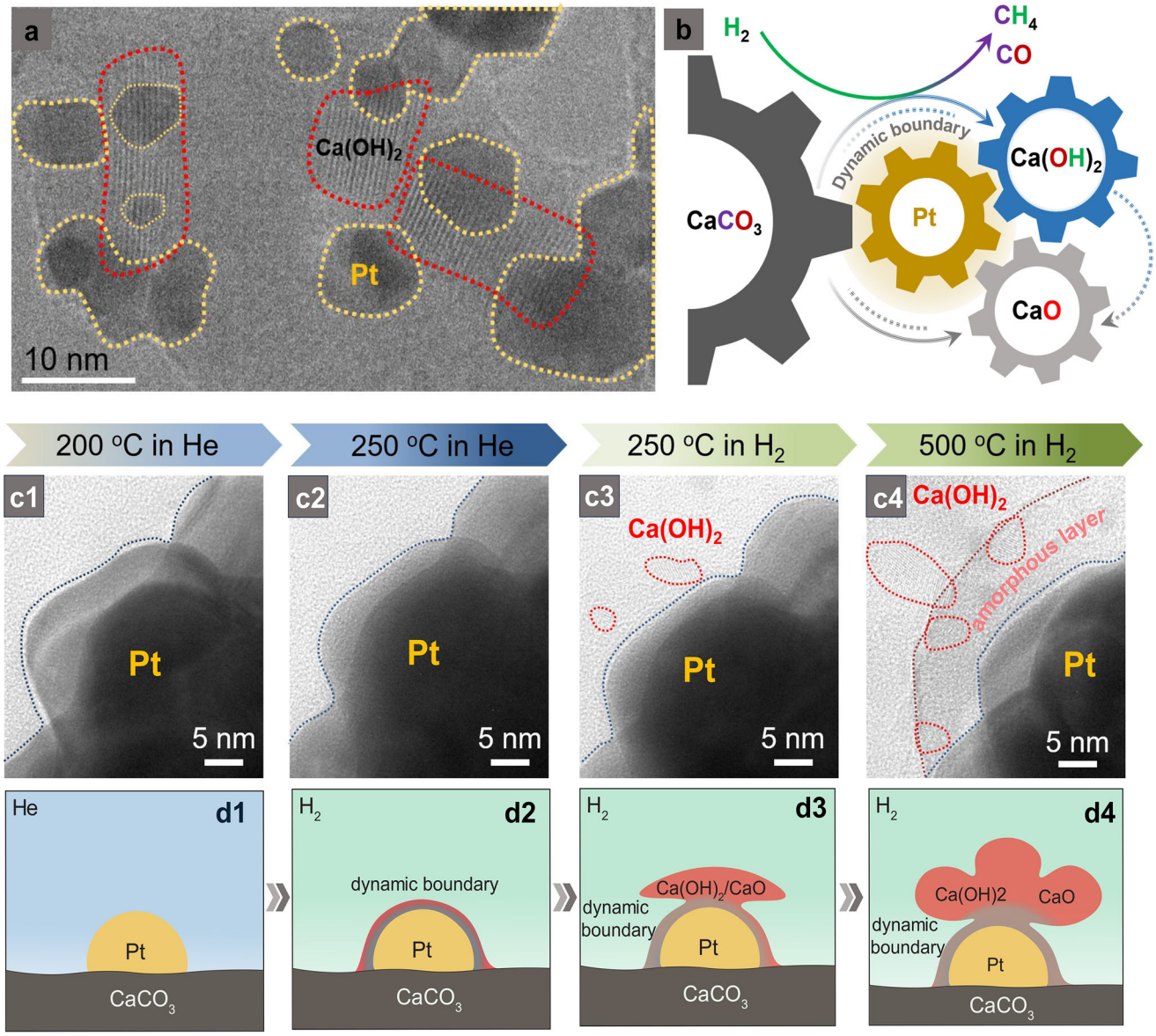

FIGURE 3 | Dynamic evolution of new solid phases and phase-boundaries. (a) Cyro-TEM image of Pt/$CaCO_3$ hydrogenated in H_2 for 2 h at 500°C. (b) Schematic illustration of catalytic hydrogenation of calcium carbonate to calcium (hydro)oxide and C_1 gaseous species. (c) In situ transmission electron microscopic images of Pt black mixed with $CaCO_3$ under He and H_2 flow at different temperatures. (d) Schematic illustration of the evolution of phases and phase-boundaries.

an interfacial layer between Pt and $CaCO_3$. At an increased electron radiation dosage of ~7000 e $Å^{-2}$ s^{-1}, the outer layer around Pt nanoparticles dissipated (Figure S17), likely due to its instability under extreme conditions. This finding informed our experimental design, allowing us to conduct in situ TEM at elevated dosage to capture dynamic solid-solid interface evolution while maintaining core structural integrity. Figure 3c1,2 show that Pt black surfaces remain clean from 200°C to 250°C in a He atmosphere. At 250°C, switching the flow from He to H_2 led to the formation of $Ca(OH)_2$ grains, highlighted by red curves in Figure 3c3, indicating Pt-catalyzed hydrogenation of $CaCO_3$ at low temperatures. This is unusual given the limited contact in the physical mixture of Pt black and carbonates with large grains (hundreds of nanometers in size), suggesting a mechanism transferring carbonate to Pt surfaces. As temperature increased to 500°C, $Ca(OH)_2$ grains grew larger (Figure 3c4). These observations challenge the tandem catalysis mechanism of sequential carbonate decomposition followed by CO_2 hydrogenation, typically occurring above 500°C [30]. An amorphous layer highlighted between red and blue curves was observed outside Pt black, suggesting interaction with Pt surfaces to reduce surface energy, subsequently converting to crystallized $Ca(OH)_2$. It is safe to deduce that the same process governs small Pt nanoparticles as their high surface free energy facilitates outside layer formation and promotes interfacial restructuring. Crucially, this interphase remains permeable to H_2 (Figure S18), allowing H_2 spill-in and Pt–H (Pt–D) formation while admitting carbonate species. Complementary CO-DRIFTS measurements (Figure S19) provide direct evidence for this permeability: after hydrogenation at elevated temperatures, both linear and bridged adsorbed CO species remain detectable on Pt surfaces, indicating that the SMRSI layer does not block reactant access. Moreover, the increased fraction of

15213773, 2026, 24, Downloaded from https://onlinelibrary.wiley.com/doi/10.1002/anie.783925 by Yonghai Cao - South China University Of Technology , Wiley Online Library on [17/11/2026]. See the Terms and Conditions (https://onlinelibrary.wiley.com/terms-and-conditions) on Wiley Online Library for rules of use; OA articles are governed by the applicable Creative Commons License

bridged adsorbed CO after hydrogenation suggests a modified Pt–support interfacial environment. Together with the spectroscopy above, these observations define a permeable, mobile amorphous interphase that encapsulates Pt and shuttles lattice CO_3^{2-} to active sites, that is, a strong metal-reactive support interaction (SMRSI).

Figure 3d1–4 schematically illustrates the dynamic process governed by SMRSI. At the outset, Pt nanoparticles contact $CaCO_3$ directly (Figure 3d1); upon exposure to H_2 at ~250°C, carbonate species at the Pt|$CaCO_3$ interface are activated by H atoms adsorbed on Pt adjacent to support, triggering the reaction through direct interfacial hydrogenation rather than hydrogen spillover into the carbonate lattice due to the highly unfavorable H spillover on nonreducible support [37]. The hydrogenated interface species then migrate onto Pt, generating a porous layer that evolves into a permeable amorphous CaO/$Ca(OH)_2$ interphase (Figure 3d2). This interfacial restructuring immediately establishes a strong concentration gradient, driving carbonate ion diffusion from the bulk toward the Pt surface. The observation confirms that H_2 serves an integrated, dual function as both a consumable reactant and initiator of interfacial mobility, consistent with adsorbate-mediated SMSI behavior reported for Rh/oxide systems [44]. With increasing temperature, this amorphous skin crystallizes while fresh lattice carbonate is continually delivered to Pt, and the newly formed $Ca(OH)_2$/CaO product displaces from the contact zone, thereby keeping the triple-phase boundary mobile (Figure 3d3,4). The need for such mobility is metal specific: without Pt, CaO can self-catalyze H_2 activation with less boundary motion; with Pt present, boundary displacement and sustained reactant delivery become rate enabling once the immediate interfacial carbonate is depleted.

In systems where CaO alone mediates H_2 activation, conversion can proceed with limited interfacial motion because new CaO sites continuously nucleate and assist gas-phase CO_2 hydrogenation. By contrast, when Pt is the active metal, the primary turnover zone is the Pt|$CaCO_3$|$Ca(OH)_2$/CaO boundary, and sustained activity demands mobility of this boundary: lattice carbonate must be delivered to Pt while the emergent $Ca(OH)_2$/CaO layer is continuously displaced from the contact zone [30]. This is precisely the role of the reactant-transporting interphase uncovered here, an amorphous, permeable layer that both encapsulates Pt and shuttles CO_3^{2-} to metal sites, thereby enabling sub-decomposition-temperature methanation with a wide high-selectivity window and re-carbonation-enabled cycling. Conceptually, this extends the functions of metal-support interaction from electronic/structural tuning to reactant transport at a mobile triple-phase boundary, offering a new design knob for solid–solid@fluid catalysis. Importantly, this mechanism is distinct from recently reported reactive SMSI in Ni/$BaCO_3$, where a porous carbonate overlayer stabilizes Ni and enriches interfacial CO_2(g) to facilitate CO_2 methanation, rather than delivering lattice carbonate to metal sites. In addition, the exceptional ~98% CH_4 selectivity under SMRSI diverges from classical SMSI behavior, where encapsulation typically favors CO formation through site blocking and reduced H_2 activation [44]. From a thermodynamic perspective, both gas-phase CO_2 hydrogenation [54] and carbonate hydrogenation (Figure S4) favor CH_4 formation at medium-low temperatures. Therefore, the selectivity differences observed in literature are primarily governed by kinetic and adsorption effects rather than thermodynamic constraints. In classical SMSI (ASMSI) states, encapsulation layers typically hinder reactant adsorption on the metal surface while facilitating CO desorption [44]. The SMRSI system exhibits fundamentally different interfacial properties that explain its unique selectivity profile. First, in situ TEM (Figure S18) and CO-DRIFTS (Figure S19) evidence confirm that the SMRSI overlayer is H_2-permeable, ensuring efficient H_2 activation on Pt nanoparticles and maintaining high H* coverage necessary for deep hydrogenation. Second, carbonate hydrogenation inherently provides CO_2 at the Pt|$Ca(OH)_2$/CaO interface through surface carbonate species, eliminating diffusion limitations that plague gas-phase CO_2 hydrogenation under encapsulation. Third, CO-DRIFTS results demonstrate that SMRSI formation enhances bridge-bonded CO adsorption on Pt, indicating stronger CO binding compared to conventional SMSI states. This enhanced adsorption prevents premature CO desorption and enables further hydrogenation to CH_4. Collectively, the combination of H_2-permeability, internal CO_2 supply from the carbonate reservoir, and enhanced CO adsorption creates an interfacial environment where both reactant adsorption and product retention are maintained. This contrasts sharply with the reactant-limited, product-facile regime characteristic of classical SMSI, explaining why SMRSI promotes deep hydrogenation rather than CO desorption.

2.4 | Mechanistic Analyses of Hydrogenation of Calcite

Quasi-situ XPS shows Pt remains predominantly metallic at 500 °C, with a persistent oxidized fraction that increases upon CO_2 exposure (Figure S20). This non-trivial oxidized component under strongly reducing conditions evidences a robust metal-reactive-support interaction with $CaCO_3$ that differs from behavior on inert supports and is probably due to an interphase that exchanges oxygen/hydroxyl species with Pt during turnover. Temperature-programmed analysis reveals two CH_4 maxima at ~415°C and 630°C (Figure 4a), mapping onto two distinct kinetic regimes with apparent activation energies of 98.9 kJ mol^{-1} at low temperature and 65.6 kJ mol^{-1} at higher temperature (Figure 4c). The low-temperature regime (E_a = 98.9 kJ mol^{-1}) corresponds to a diffusion-limited solid-state process [55, 56], where CO_3^{2-} transport through the dynamic amorphous interphase at the mobile Pt | $CaCO_3$ | $Ca(OH)_2$/CaO boundary controls the overall rate. In this regime, the high activation barrier reflects the energy required for solid-state carbonate ion migration through the evolving reaction interface.

The higher-temperature regime (E_a = 65.6 kJ mol^{-1}) exhibits a lower activation energy comparable to metal-catalyzed CO_2 hydrogenation [19], which does not arise from bulk $CaCO_3$ decomposition but rather reflects a mixed regime involving accelerated CO_3^{2-} diffusion and localized interfacial CO_2 generation at Pt–support contacts. This localized CO_2 formation is catalyzed by Pt at the interface, as evidenced by the low-temperature CO_2 release feature at ~435°C in thermogravimetric analysis (Figure 4d), which occurs well below the bulk decomposition temperature. This shift in rate-determining step occurs as interfacial CO_2 release becomes kinetically accessible, facilitated by nanoconfinement effects and enhanced reactivity at the Pt–$CaCO_3$ contact points. The wide 380–520°C window with ~98%

15213773, 2026, 24, Downloaded from https://onlinelibrary.wiley.com/doi/10.1002/anie.7839925 by Yonghai Cao - South China University Of Technology , Wiley Online Library on [17/11/2026]. See the Terms and Conditions (https://onlinelibrary.wiley.com/terms-and-conditions) on Wiley Online Library for rules of use; OA articles are governed by the applicable Creative Commons License

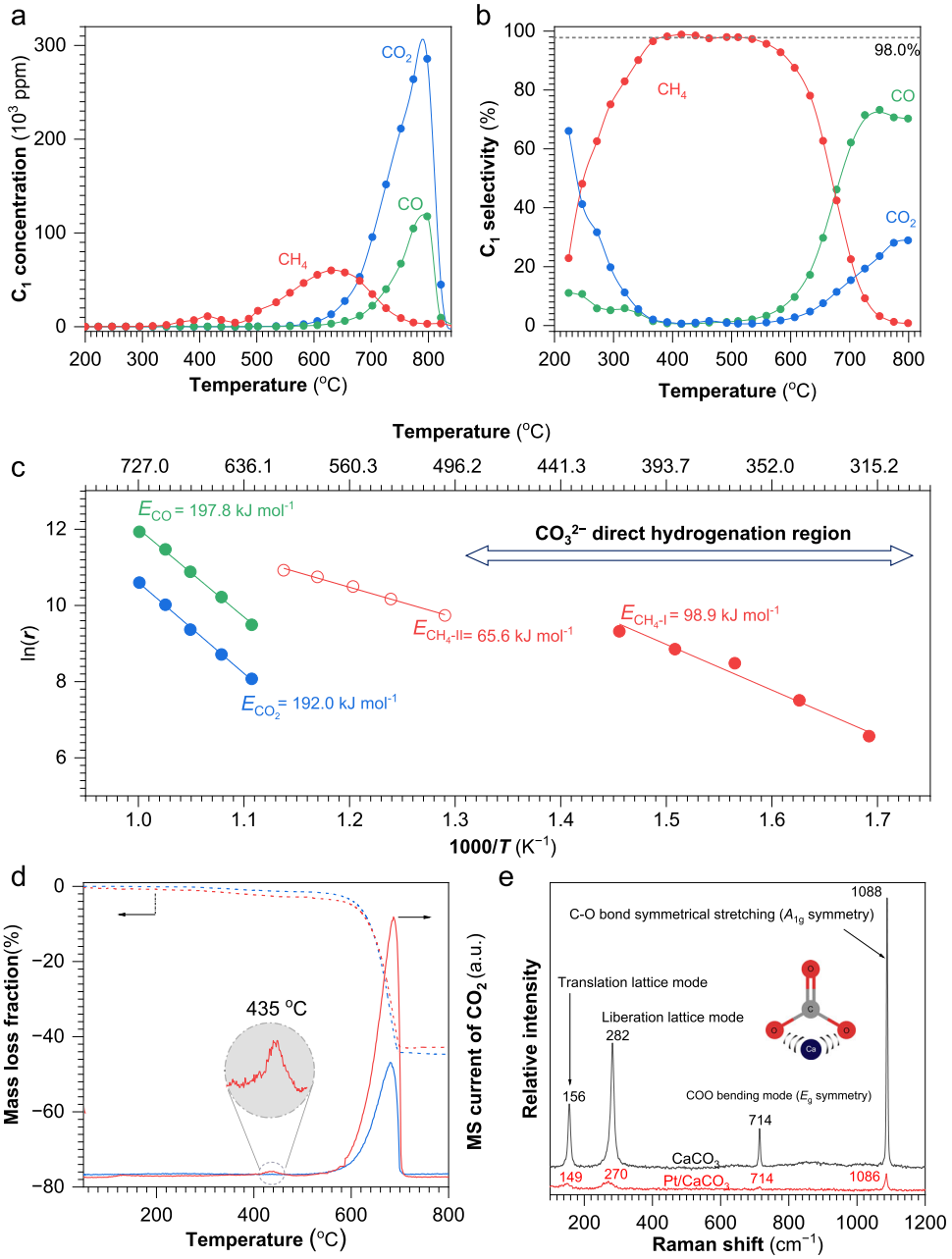

FIGURE 4 | Reaction kinetics of catalytic hydrogenation of $CaCO_3$. (a) Concentration and (b) selectivity of products during hydrogenation of $Pt/CaCO_3$ as a function of temperature under the H_2 flow (5 mL min^{-1}). (c) Arrhenius plots of different gas products in varied temperature range extract from (a and c). Thermogravimetric-mass curves of $CaCO_3$ (blue) and $Pt/CaCO_3$ (red) in Ar atmosphere. (d) Raman spectra of $CaCO_3$ and $Pt/CaCO_3$.

CH_4 selectivity demonstrates that when lattice carbonate supply is sustained, complete hydrogenation to CH_4 is kinetically favored at the interface.

Thermogravimetric-mass spectrometry under Ar displays two CO_2 release features (Figure 4d): a low-temperature peak at ~435°C, indicative of interfacial decarbonation promoted by Pt, and a high-temperature peak at ~660°C corresponding to bulk $CaCO_3$ decomposition. The low-temperature CO_2 evolution, occurring significantly below the bulk decomposition threshold, confirms that Pt catalyzes carbonate activation at the interface. Concomitant Raman redshifts of lattice/translational modes (Figure 4e) reveal weakened restoring forces on surface CO_3^{2-} near Pt, providing spectroscopic evidence for boundary activation.

Together with the observation of a *CO to CH_4 sequence (Figure 2d), these results anchor a carbonate-derived carbon pathway operating below the bulk $CaCO_3$ decomposition limit. The Arrhenius analysis yields apparent activation energies of 98.9 and 65.6 kJ mol^{-1} for the low- and high-temperature regimes, respectively, reflecting temperature-dependent changes in the rate-determining step. The higher value in the temperature range 318–415 °C aligns with solid-state carbonate ion diffusion during calcite decomposition, where consumption of CO_3^{2-}, at Pt creates a local chemical potential gradient driving lattice-to-interface flux

15213773, 2026, 24, Downloaded from https://onlinelibrary.wiley.com/doi/10.1002/anie.783925 by Yonghai Cao - South China University Of Technology , Wiley Online Library on [17/11/2026]. See the Terms and Conditions (https://onlinelibrary.wiley.com/terms-and-conditions) on Wiley Online Library for rules of use; OA articles are governed by the applicable Creative Commons License

[56]. As elevated temperature to 502–605°C, SMRSI continues to operate with accelerated CO_3^{2-} diffusion. In addition, thermal decomposition of active interfacial carbonates may generate free CO_2, which can be supported by the low-temperature CO_2 release at ~435°C in thermogravimetric analysis (Figure 4d). Thus, surface hydrogenation of intermediates from CO_3^{2-} and the localized interfacial CO_2 becomes rate-determining, displaying a reduced $E_a = 65.6$ kJ mol^{-1}. Although this value is consistent with the apparent activation energy for gas-phase CO_2 hydrogenation [57], it does not involve the bulk $CaCO_3$ decomposition, which exhibits a substantially higher activation energy, rather reflecting the catalytic decomposition of active interfacial carbonate in this temperature range. Activation energies for CO_2 and CO formation (192.0 kJ mol^{-1} and 197.8 kJ mol^{-1}, respectively) confirm that bulk $CaCO_3$ decomposition dominates only at higher temperatures [18, 30].

Above 630°C, CH_4 production declines due to unfavorable thermodynamics (Figure S4), consistent with the high-temperature CO_2 release peak and increased bulk decomposition pathways. These orthogonal lines of evidence converge on a SMRSI mechanism: under H_2, Pt nucleates a permeable amorphous interphase that dynamically encapsulates the metal, continuously shuttling lattice CO_3^{2-} to active sites, and displaces $Ca(OH)_2$/CaO from the contact zone, thereby maintaining a mobile triple-phase boundary. This transport-enabled interface rationalizes the low onset temperature (≤ 415°C), the broad high-selectivity window, and the re-carbonation-enabled cycling stability.

Different from previous reported MSI [41], the interphase's primary function is delivery of lattice carbonate to metal sites, not enrichment/storage of gaseous CO_2. This difference in reactant identity, mass-transport direction, and kinetic control underpins the conceptual advance from SMSI (tuning/stabilization) to SMRSI (reactant transport at moving interfaces). Through advanced in situ characterization techniques, we have elucidated the complete dynamic process of solid-phase carbonate migration, activation, and transformation on Pt surfaces. Under mild conditions (250°C), $CaCO_3$ forms a permeable amorphous intermediate layer driven by interfacial energy, which crystallizes into $Ca(OH)_2$ nanoparticles while releasing CO_3^{2-} species that are hydrogenated to methane with exceptional selectivity at platinum active sites. Kinetic studies reveal a dual-path mechanism: the low-temperature regime (<415°C) is dominated by bulk CO_3^{2-} diffusion (activation energy of 98.9 kJ mol^{-1}), while the high-temperature regime (>530°C) exhibits a lower activation energy 65.6 kJ mol^{-1}, consistent with a mixed pathway involving accelerated solid-state carbonate delivery and localized interfacial CO_2 hydrogenation.

3 | Conclusion

This work establishes a transport-enabled SMRSI that converts lattice carbonate directly to methane at moving solid–solid@gas boundaries, thereby opening the black box of solid-reactant catalysis. On Pt/$CaCO_3$ under H_2, a permeable amorphous interphase forms at the Pt|$CaCO_3$ contact, dynamically encapsulates Pt, shuttles CO_3^{2-} to active sites, and displaces nascent $Ca(OH)_2$/CaO to keep the boundary mobile, delivering sub-decomposition-temperature activity (onset ≤415 °C) via direct carbonate delivery, alongside a broad ~98% CH_4 selectivity window (390–510 °C). This temperature-dependent kinetic behavior supports this mechanistic framework. A higher activation energy at lower temperatures is consistent with solid-state CO_3^{2-} diffusion whereas the lower activation energy at higher temperatures arises from accelerated carbonate delivery and localized interfacial CO_2 hydrogenation. CO_2-driven re-carbonation regenerates $CaCO_3$, enabling sustained cycling. Under hydrogen, Pt induces a permeable amorphous interphase that encapsulates the metal, continuously delivers carbonate to active sites, and clears products, enabling low-temperature, highly selective operation and re-carbonation-enabled cycling.

Conceptually, SMRSI advances MSI from electronic/structural [58, 59] tuning to mass-transport functionality, providing simple descriptors such as interfacial permeability and boundary mobility for designing catalysts in which the support is also the reactant. Beyond calcite, the framework offers broadly applicable guidance for solid–solid@fluid catalysis and suggests a practical route to an accelerated carbonate cycle using green hydrogen.

4 | Materials and Methods

4.1 | Methods

4.1.1 | Synthesis of Pt/$CaCO_3$

The Pt/$CaCO_3$ hydrogenation catalyst was synthesized through a two-step procedure. In the first step, Pt nanoparticles with an average size of approximately 3 nm were prepared by dissolving 510 mg (12.75 mmol) of NaOH and 1007 mg (2.24 mmol) of $H_2PtCl_6{\cdot}6H_2O$ separately in 50 mL portions of ethylene glycol. The two solutions were then combined in a glass flask to form a 100 mL reaction mixture containing 0.04 M Pt and 0.26 M NaOH. This mixture was heated from room temperature to 160°C under an argon atmosphere (flow rate: 120 mL min^{-1}) with vigorous stirring at 800 rpm, and maintained at this temperature for 3 h to complete the nanoparticle formation. In the second step, the as-synthesized Pt nanoparticles were supported on $CaCO_3$ by adding the carrier material in an amount corresponding to 5 wt.% Pt loading to the nanoparticle suspension, followed by continuous stirring for 24 h. The resulting material was thoroughly purified through 20 cycles of centrifugation washing with deionized water (Millipore Milli-Q, resistivity: 18.25 MΩ·cm). For in situ TEM characterization, a control sample was prepared by simple physical mixing of commercial micro-sized Pt black powder with $CaCO_3$ powder.

4.1.2 | Catalytic Performance Tests of Pt/$CaCO_3$

The hydrogenation experiments were conducted in a quartz tubular fixed-bed reactor (9.6 mm inner diameter × 330 mm length) heated by a tube furnace. For each test, 250 mg of Pt/$CaCO_3$ catalyst was loaded into the reactor's constant temperature zone, with reaction temperatures monitored using a 3 mm diameter K-type thermocouple. The system was initially purged with N_2 (50 Ncm^3 min^{-1}) for 30 min to remove air, followed by heating to 200 at 10°C min^{-1} under continuous N_2 flow. Upon temperature stabilization at 200°C, the feed gas was switched to

15213773, 2026, 24, Downloaded from https://onlinelibrary.wiley.com/doi/10.1002/anie.783992 5 by Yonghai Cao - South China University Of Technology , Wiley Online Library on [17/11/2026]. See the Terms and Conditions (https://onlinelibrary.wiley.com/terms-and-conditions) on Wiley Online Library for rules of use; OA articles are governed by the applicable Creative Commons License

H_2 or H_2/N_2 mixtures (5–50 Ncm^3 min^{-1}). The temperature was then programmed to increase to 800°C at 4°C min^{-1}. Effluent gases were sampled every 6 min and analyzed by online gas chromatography (Fuli 9790, Taizhou, China) equipped with: (1) a TDX-01 packed column, (2) a flame ionization detector (FID), and (3) a thermal conductivity detector (TCD) for comprehensive analysis of C_1 products. The selectivity of C_1 products, *i.e.*, S_i, was calculated by formula (1).

$$S_i = \frac{c_{i,\text{out}}}{c_{\text{CH}_4,\text{out}} + c_{\text{CO,out}} + c_{\text{CO}_2,\text{out}}} \times 100\% \quad (1)$$

wherein c_i repsrented concentration of C_1 products. The cumulative conversion of $CaCO_3$ (X_{CaCO3}) was calculated according to formula (2).

$$X_{\text{CaCO}_3} = \frac{n_{\text{CH}_4,\text{out}} + n_{\text{CO,out}} + n_{\text{CO}_2,\text{out}}}{n_{\text{CaCO}_3,\text{in}}} \times 100\% \quad (2)$$

When performing the cyclic test of hydrogenation–carbonation, the bed of $Pt/CaCO_3$ was heated to 500°C under 50 Ncm^3 min^{-1} N_2 and was hydrogenated under H_2 with the flow rate of 5 Ncm^3 min^{-1}. Thirty minutes, thereafter, the gas flow was switched to N_2 with the flow rate 300 Ncm^3 min^{-1} and purged for 10 min, and subsequently switched to 10% CO_2/N_2 of 30 Ncm^3 min^{-1} for carbonation. 10 min thereafter, the gas flow was switched to 300 Ncm^3 min^{-1} N_2 again and purged for 10 min, and the gas flow was then switched back to 5 Ncm^3 min^{-1} H_2. The production rate of CH_4 in the cyclic test (r_{CH4}) was calculated by Formula (3).

$$r_{\text{CH}_4} = \frac{n_{\text{CH}_4,\text{out}}}{m_{\text{Pt}} t} \quad (3)$$

Author Contributions

H. Y. and G. Y. conceived and supervised the project. G.Y., H. L., and C. D conducted the experiments. Y. N. and B. Z. performed in situ TEM tests. C. Y., H.-F. W., H. W., and F. P. analyzed and discussed the results. G. Y. and H. Y. wrote the paper.

Acknowledgments

This work was supported by the National Natural Science Foundation of China (No. 22078106 and No. 22008076) and the Natural Science Foundation of Guandong Province (No. 2024B1515040016).

Conflicts of Interest

The authors declare no conflicts of interest.

Data Availability Statement

The data that support the findings of this study are available from the corresponding author upon reasonable request.

References

1. R. A. Berner, "The Long-Term Carbon Cycle, Fossil Fuels and Atmospheric Composition," *Nature* 426, no. 6964 (2003): 323–326, https://doi.org/10.1038/nature02131.

2. P. Friedlingstein, M. W. Jones, M. O'Sullivan, et al., "Global Carbon Budget 2021," *Earth System Science Data* 14, no. 4 (2022): 1917–2005, https://doi.org/10.5194/essd-14-1917-2022.

3. Y. Zhu, J. Wang, Y. Ou, et al., "Asymmetric Electrosorption in a Bio-Inspired Reactor Enables Energy Efficient Ocean Carbon Removal," *Angewandte Chemie International Edition* 64, no. 49 (2025): e202515007, https://doi.org/10.1002/anie.202515007.

4. Y.-O. He, W.-Y. Zheng, Y. Liu, et al., "Direct Air Capture and Photoconversion of CO_2 to Ethylene by Defect-Tailored Cu_3-Based Metal–Organic Frameworks," *Angewandte Chemie International Edition* 65, no. 5 (2026): e16438, https://doi.org/10.1002/anie.202516438.

5. Z. Zhou, T. Ma, H. Zhang, et al., "Carbon Dioxide Capture From Open Air Using Covalent Organic Frameworks," *Nature* 635, no. 8037 (2024): 96–101, https://doi.org/10.1038/s41586-024-08080-x.

6. A.-C. Zheng, Y.-B. Zou, L. Du, Q. Zhang, K. Daasbjerg, and X.-M. Hu, "Efficient Direct Air Capture in Industrial Cooling Towers Mediated by Electrochemical CO_2 Release," *Angewandte Chemie International Edition* 64, no. 5 (2025): e202412697, https://doi.org/10.1002/anie.202412697.

7. T. T. Isson, N. J. Planavsky, L. A. Coogan, et al., "Evolution of the Global Carbon Cycle and Climate Regulation on Earth," *Global Biogeochemical Cycles* 34, no. 2 (2020): e2018GB006061.

8. J. R. Zondervan, R. G. Hilton, M. Dellinger, F. J. Clubb, T. Roylands, and M. Ogrič, "Rock Organic Carbon Oxidation CO_2 Release Offsets Silicate Weathering Sink," *Nature* 623, no. 7986 (2023): 329–333, https://doi.org/10.1038/s41586-023-06581-9.

9. A. Reller, C. Padeste, and P. Hug, "Formation of Organic Carbon Compounds From Metal Carbonates," *Nature* 329, no. 6139 (1987): 527–529, https://doi.org/10.1038/329527a0.

10. A. A. Giardini, C. A. Salotti, and J. F. Lakner, "Synthesis of Graphite and Hydrocarbons by Reaction Between Calcite and Hydrogen," *Science* 159, no. 3812 (1968): 317–319, https://doi.org/10.1126/science.159.3812.317.

11. D. Zhang, H. Li, Q. Wu, et al., "Techno-Economic Analysis of Hydrogen-Driven Calcium Looping Process for Flue Gas Decarbonization," *Carbon Future* 1, no. 4 (2024): 9200023, https://doi.org/10.26599/CF.2024.9200023.

12. Z. Xue, J. Guo, S. Wu, et al., "Co-Thermal in-situ Reduction of Inorganic Carbonates to Reduce Carbon-Dioxide Emission," *Science China Chemistry* 66, no. 4 (2023): 1201–1210, https://doi.org/10.1007/s11426-022-1537-6.

13. S. Lux, G. Baldauf-Sommerbauer, and M. Siebenhofer, "Hydrogenation of Inorganic Metal Carbonates: A Review on its Potential for Carbon Dioxide Utilization and Emission Reduction," *Chemsuschem* 11, no. 19 (2018): 3357–3375, https://doi.org/10.1002/cssc.201801356.

14. X. Jiang, X. Nie, X. Guo, C. Song, and J. G. Chen, "Recent Advances in Carbon Dioxide Hydrogenation to Methanol via Heterogeneous Catalysis," *Chemical Reviews* 120, no. 15 (2020): 7984–8034, https://doi.org/10.1021/acs.chemrev.9b00723.

15. R. Ye, J. Ding, T. R. Reina, et al., "Design of Catalysts for Selective CO_2 Hydrogenation," *Nature Synthesis* 4 (2025): 288–302, https://doi.org/10.1038/s44160-025-00747-1.

16. J. Ye, N. Dimitratos, L. M. Rossi, N. Thonemann, A. M. Beale, and R. Wojcieszak, "Hydrogenation of CO_2 for Sustainable Fuel and Chemical Production," *Science* 387, no. 6737 (2025): eadn9388, https://doi.org/10.1126/science.adn9388.

17. K. S. P. Karunadasa, C. H. Manoratne, H. M. T. G. A. Pitawala, and R. M. G. Rajapakse, "Thermal Decomposition of Calcium Carbonate (calcite polymorph) as Examined by in-situ High-Temperature X-Ray Powder Diffraction," *Journal of Physics and Chemistry of Solids* 134 (2019): 21–28, https://doi.org/10.1016/j.jpcs.2019.05.023.

18. A. W. D. Hills, "The Mechanism of the Thermal Decomposition of Calcium Carbonate," *Chemical Engineering Science* 23, no. 4 (1968): 297–320, https://doi.org/10.1016/0009-2509(68)87002-2.

19. M. A. A. Aziz, A. A. Jalil, S. Triwahyono, and A. Ahmad, "CO_2 Methanation Over Heterogeneous Catalysts: Recent Progress and Future Prospects," *Green Chemistry* 17, no. 5 (2015): 2647–2663, https://doi.org/10.1039/C5GC00119F.

15213773, 2026, 24, Downloaded from https://onlinelibrary.wiley.com/doi/10.1002/anie.783992 5 by Yonghai Cao - South China University Of Technology , Wiley Online Library on [17/11/2026]. See the Terms and Conditions (https://onlinelibrary.wiley.com/terms-and-conditions) on Wiley Online Library for rules of use; OA articles are governed by the applicable Creative Commons License

20. P. Jiang, L. Li, G. Zhao, et al., "Reductive Calcination of Calcium Carbonate in Hydrogen and Methane: A Thermodynamic Analysis on Different Reaction Routes and Evaluation of Carbon Dioxide Mitigation Potential," *Chemical Engineering Science* 276 (2023): 118823, https://doi.org/10.1016/j.ces.2023.118823.

21. B. Jin, D. Fu, X. Xiang, et al., "Integrated Metal Carbonate Thermal Decomposition With in-Situ CO_2 Conversion: Review and Perspective," *Gas Science and Engineering* 129 (2024): 205416, https://doi.org/10.1016/j.jgsce.2024.205416.

22. A. Loder, M. Siebenhofer, A. Böhm, and S. Lux, "Clean Iron Production Through Direct Reduction of Mineral Iron Carbonate With Low-Grade Hydrogen Sources; the Effect of Reduction Feed Gas Composition on Product and Exit Gas Composition," *Cleaner Engineering and Technology* 5 (2021): 100345, https://doi.org/10.1016/j.clet.2021.100345.

23. G.-C. Mao, X.-T. Kan, M.-X. Xiao, W.-L. Liu, B.-X. Dong, and Y.-L. Teng, "Alkaline Earth Metal-Induced Hydrogenation of the CaO-Captured CO_2 to Methane at Room Temperature," *Industrial & Engineering Chemistry Research* 61, no. 28 (2022): 10124–10132.

24. C. Mesters, N. Rahimi, D. van der Sloot, J. Rhyne, and F. Cassiola, "Direct Reduction of Magnesium Carbonate to Methane," *ACS Sustainable Chemistry & Engineering* 9, no. 33 (2021): 10977–10989, https://doi.org/10.1021/acssuschemeng.1c01439.

25. Y. Shan, P. Wang, S. Ma, and T. Song, "Hydrogenation of Magnesite to Methane and Magnesium Oxide With a Ferromagnetic Catalyst Toward CO_2 Direct Utilization," *Industrial & Engineering Chemistry Research* 62, no. 47 (2023): 20202–20212, https://doi.org/10.1021/acs.iecr.3c03179.

26. S. Shi, J. Yu, Y. Pan, et al., "Hydrogenation of Calcium Carbonate to Carbon Monoxide and Methane," *Fuel* 354 (2023): 129385, https://doi.org/10.1016/j.fuel.2023.129385.

27. S. Shi, Y. Zhang, Y. Pan, et al., "Hydrogenation of $CaCO_3$ to CH_4 Catalyzed by $NiCO_3$," *Chemical Engineering Journal* 485 (2024): 150012, https://doi.org/10.1016/j.cej.2024.150012.

28. P. Wang, Y. Shan, and T. Song, "Catalytic Hydrogenation of Magnesite to Methane and Magnesium Oxide Using Magnesium Carbonate Hydroxide as Model Compound," *International Journal of Hydrogen Energy* 84 (2024): 1033–1041, https://doi.org/10.1016/j.ijhydene.2024.08.335.

29. A. A. Giardini and C. A. Salotti, "Kinetics and Relations in the Calcite-Hydrogen Reaction and Relations in the Dolomite-Hydrogen and Siderite-Hydrogen Systems," *American Mineralogist* 54, no. 7-8 (1969): 1151–1172.

30. J. Shen, X. Cheng, W. Wei, X. Tian, and M. Ding, "Insights Into the Mechanism of in Situ CO_2 Conversion During $CaCO_3$ Hydrogenation," *ACS Catalysis* 15, no. 3 (2025): 2402–2414, https://doi.org/10.1021/acscatal.4c07463.

31. C. Padeste, H. R. Oswald, and A. Reller, "The Thermal Behaviour of Pure and Nickel-Doped Hydromagnesite in Different Atmospheres," *Materials Research Bulletin* 26, no. 12 (1991): 1263–1268, https://doi.org/10.1016/0025-5408(91)90140-H.

32. D. Jagadeesan, M. Eswaramoorthy, and C. N. R. Rao, "Investigations of the Conversion of Inorganic Carbonates to Methane," *Chemsuschem* 2, no. 9 (2009): 878–882, https://doi.org/10.1002/cssc.200900152.

33. X. Ma, X. Li, H. Cui, W. Zhang, Z. Cheng, and Z. Zhou, "Metal Oxide-Doped Ni/ CaO Dual-Function Materials for Integrated CO_2 Capture and Conversion: Performance and Mechanism," *AIChE Journal* 69, no. 1 (2023): e17520, https://doi.org/10.1002/aic.17520.

34. R. Prins, "Hydrogen Spillover. Facts and Fiction," *Chemical Reviews* 112, no. 5 (2012): 2714–2738, https://doi.org/10.1021/cr200346z.

35. M. M. Bettahar, "The Hydrogen Spillover Effect. A Misunderstanding Story," *Catalysis Reviews* 64, no. 1 (2022): 87–125, https://doi.org/10.1080/01614940.2020.1787771.

36. R. Prins, V. K. Palfi, and M. Reiher, "Hydrogen Spillover to Nonreducible Supports," *The Journal of Physical Chemistry C* 116, no. 27 (2012): 14274–14283, https://doi.org/10.1021/jp212274y.

37. W. Karim, C. Spreafico, A. Kleibert, et al., "Catalyst Support Effects on Hydrogen Spillover," *Nature* 541, no. 7635 (2017): 68–71, https://doi.org/10.1038/nature20782.

38. Z.-K. Guo, H.-Q. Chen, H.-L. Jiang, B.-X. Dong, and Y.-L. Teng, "Selective Conversion of the CaO-Captured CO_2 to CH_4 by Ni- and Hydrogen-Assisted Calcium Looping Processes in a Batch Reactor," *The Journal of Physical Chemistry C* 127, no. 5 (2023): 2173–2182, https://doi.org/10.1021/acs.jpcc.2c07619.

39. H. Sun, Y. Wang, S. Xu, et al., "Understanding the Interaction Between Active Sites and Sorbents During the Integrated Carbon Capture and Utilization Process," *Fuel* 286 (2021): 119308.

40. T. T. Belete, M. C. M. van de Sanden, and M. A. Gleeson, "Effects of Transition Metal Dopants on the Calcination of $CaCO_3$ Under Ar, H_2O and H_2," *Journal of CO2 Utilization* 31 (2019): 152–166.

41. W. Zhang, D. Li, C. Liu, et al., "Facilitated CO_2 Hydrogenation by Strong Metal-Support Interaction between Ni and $BaCO_3$," *Chem Catalysis* 4, no. 10 (2024): 101113, https://doi.org/10.1016/j.checat.2024.101113.

42. S. Fukushima, Y. Horibe, and T. Titani, "A Study on the Mechanism of the Catalytic Action of Manganese Dioxide on the Decomposition of Potassium Chlorate by Use of Heavy Oxygen as an Isotopic Tracer," *Bulletin of the Chemical Society of Japan* 25, no. 4 (1952): 245–248, https://doi.org/10.1246/bcsj.25.245.

43. F. E. Brown, J. A. Burrows, and H. M. McLaughlin, "The Decomposition of Potassium Chlorate. I. Spontaneous Decomposition Temperatures of Mixtures of Potassium Chlorate and Manganese Dioxide," *Journal of the American Chemical Society* 45, no. 6 (1923): 1343–1348, https://doi.org/10.1021/ja01659a001.

44. J. C. Matsubu, S. Zhang, L. DeRita, et al., "Adsorbate-Mediated Strong Metal–Support Interactions in Oxide-Supported Rh Catalysts," *Nature Chemistry* 9, no. 2 (2017): 120–127, https://doi.org/10.1038/nchem.2607.

45. Y. Liu, Y. An, C. Fang, et al., "Surface-Localized Phase Mediation Accelerates Quasi-Solid-State Reaction Kinetics in Sulfur Batteries," *Nature Chemistry* 17 (2025): 614–623.

46. R. Becka, S. Bajohr, and T. Kolb, "Review on CO_2 Activation via Catalytic Reverse Water-Gas Shift Reaction," *Chemie Ingenieur Technik* 97, no. 8-9 (2025): 860–881, https://doi.org/10.1002/cite.70013.

47. Q. Wu, H. Li, G. Yang, et al., "Surface Intermediates Steer the Pathways of CO_2 Hydrogenation on Pt/γ-Al_2O_3: Importance of the Metal-Support Interface," *Journal of Catalysis* 425 (2023): 40–49, https://doi.org/10.1016/j.jcat.2023.05.028.

48. D. Paleček, G. Tek, J. Lan, M. Iannuzzi, and P. Hamm, "Characterization of the Platinum–Hydrogen Bond by Surface-Sensitive Time-Resolved Infrared Spectroscopy," *The Journal of Physical Chemistry Letters* 9, no. 6 (2018): 1254–1259.

49. M. Carosso, E. Vottero, A. Lazzarini, et al., "Dynamics of Reactive Species and Reactant-Induced Reconstruction of Pt Clusters in Pt/Al_2O_3 Catalysts," *ACS Catalysis* 9, no. 8 (2019): 7124–7136, https://doi.org/10.1021/acscatal.9b02079.

50. W. Sekkal and A. Zaoui, "Nanoscale Analysis of the Morphology and Surface Stability of Calcium Carbonate Polymorphs," *Scientific Reports* 3, no. 1 (2013): 1587, https://doi.org/10.1038/srep01587.

51. R. Tran, Z. Xu, B. Radhakrishnan, et al., "Surface Energies of Elemental Crystals," *Scientific Data* 3, no. 1 (2016): 160080.

52. C. Rodriguez-Navarro, E. Ruiz-Agudo, A. Luque, A. B. Rodriguez-Navarro, and M. Ortega-Huertas, "Thermal Decomposition of Calcite: Mechanisms of Formation and Textural Evolution of CaO Nanocrystals," *American Mineralogist* 94, no. 4 (2009): 578–593, https://doi.org/10.2138/am.2009.3021.

53. R. Hooley, A. Brown, and R. Brydson, "Factors Affecting Electron Beam Damage in Calcite Nanoparticles," *Micron (Oxford, England: 1993)* 120 (2019): 25–34, https://doi.org/10.1016/j.micron.2019.01.011.

15213773, 2026, 24, Downloaded from https://onlinelibrary.wiley.com/doi/10.1002/anie.78393925 by Yonghai Cao - South China University Of Technology , Wiley Online Library on [17/11/2026]. See the Terms and Conditions (https://onlinelibrary.wiley.com/terms-and-conditions) on Wiley Online Library for rules of use; OA articles are governed by the applicable Creative Commons License

54. W. Wang, M. Nguyen-Quang, D. Mateo, et al., "A Review of CO_2 Methanation Process: Recent Advances and Future Prospects," *ACS Catalysis* 15, no. 12 (2025): 10868–10896, https://doi.org/10.1021/acscatal.5c01422.

55. S. K. Bhatia and D. D. Perlmutter, "Effect of the Product Layer on the Kinetics of the CO_2-Lime Reaction," *AIChE Journal* 29, no. 1 (1983): 79–86, https://doi.org/10.1002/aic.690290111.

56. Z. Sun, S. Luo, P. Qi, and L.-S. Fan, "Ionic Diffusion Through Calcite ($CaCO_3$) Layer During the Reaction of CaO and CO_2," *Chemical Engineering Science* 81 (2012): 164–168, https://doi.org/10.1016/j.ces.2012.05.042.

57. S. J. Park, X. Wang, M. R. Ball, L. Proano, Z. Wu, and C. W. Jones, "CO_2 Methanation Reaction Pathways Over Unpromoted and $NaNO_3$-Promoted Ru/Al_2O_3 Catalysts," *Catalysis Science & Technology* 12, no. 14 (2022): 4637–4652, https://doi.org/10.1039/D2CY00515H.

58. T. Maxson and T. Szilvási, "Metal-Support Interactions Reshape Nanoparticle Catalyst Surfaces," *Angewandte Chemie Novit* 1, no. 1 (2025): e70008, https://doi.org/10.1002/anov.70008.

59. Z.-K. Yu, M. Jiang, S. Dai, W. Zhan, Z.-Q. Wang, and X.-Q. Gong, "Valence Restrictive Metal-Support Interaction for Boosting Catalytic Activity of Rh/CeO_2 in CO_2 Hydrogenation," *Nature Communications* 16, no. 1 (2025): 9072, https://doi.org/10.1038/s41467-025-64140-4.

Supporting Information

Additional supporting information can be found online in the Supporting Information section.

Supporting File: anie72308-sup-0001-SuppMat.docx.

15213773, 2026, 24, Downloaded from https://onlinelibrary.wiley.com/doi/10.1002/anie.783992 5 by Yonghai Cao - South China University Of Technology , Wiley Online Library on [17/11/2026]. See the Terms and Conditions (https://onlinelibrary.wiley.com/terms-and-conditions) on Wiley Online Library for rules of use; OA articles are governed by the applicable Creative Commons License